High-pressure formation and characterization of a boron carbide polymorph featuring bent C–B–C chains

Akun Liang,[1,2,*] Umbertoluca Ranieri,[1] James Spender,[1] Charles Lamb,[1] Sarah Bolton,[1] Bernhard Massani,[1]
Ryan Stewart McWilliams,[1] Timofey Fedotenko,[3] Konstantin Glazyrin,[3] Nico Giordano,[3] Jonathan Wright,[4]
Florian Trybel,[5] and Dominique Laniel[1,†]
[1]*Centre for Science at Extreme Conditions and School of Physics and Astronomy,*
University of Edinburgh, Edinburgh EH8 9YL, United Kingdom
[2]*College of Science, Eastern Institute of Technology, Ningbo 315200, China*
[3]*Deutsches Elektronen-Synchrotron DESY, Notkestrasse 85, Hamburg 22607, Germany*
[4]*European Synchrotron Radiation Facility, Grenoble 38000, France*
[5]*Department of Physics, Chemistry and Biology (IFM), Linköping University, Linköping 58183, Sweden*

(Received 25 September 2025; revised 6 February 2026; accepted 20 February 2026; published 20 March 2026)

Boron carbide is a material of choice for multiple industries, e.g., aerospace, as a lightweight structural ceramic due to its high hardness, high melting temperature, and low density. However, its mechanical properties have been observed to radically degrade under shockwave compression, presumably as a consequence of stress-induced phase transitions resulting in its partial amorphization. So far, the physical mechanism underpinning this behavior remains unclear. Here, we report a pressure-induced phase transition in boron carbide occurring between 78 and 90 GPa during static compression in diamond anvil cells, both at room temperature and after quenching from high temperatures. The crystal structure of the new phase was solved and refined via synchrotron single-crystal x-ray diffraction measurements and further investigated by Raman spectroscopy as well as density functional theory calculations. The discovered high-pressure polymorph, $mC60\text{-}B_{13}C_2$, has strong resemblance with the known ambient conditions phase, $hR45\text{-}B_{13}C_2$, with the important distinction that the linear C–B–C chain linking B_{12} icosahedra in $hR45\text{-}B_{13}C_2$ is bent in $mC60\text{-}B_{13}C_2$. Such bending of the C–B–C chain has been hypothesized as key to explain boron carbide's drop in strength, phase transitions, and amorphization. The observed reversibility of the phase transition, as well as the formation of covalent bonds between B_{12} icosahedra and the bent C–B–C chains, are assessed to decipher the C–B–C chain's bending importance on the amorphization and mechanical properties of boron carbide.

DOI: 10.1103/v5kf-svcz

I. INTRODUCTION

In its various stoichiometries, boron carbide consists of B_{12} or CB_{11} icosahedra and linear three-atoms chain (C–B–C, C–C–C, or C–B–B), defect chains (C–vacancy–C) or four-atoms chains (C–B–C–B), oriented along the *c* axis of its hexagonal unit cell [1–8]. On account of its short, strong, and multidirectional covalent bonds, it features a range of exceptional mechanical properties such as superhardness (Vickers hardness of ~41 GPa) [9], a high melting temperature ($T_m > 2700$ K) [10], a low density (~2.55 g/cm^3 at ambient conditions) [11], a substantial Young's modulus (420 GPa) [12], a high Hugoniot elastic limit (HEL, ~20 GPa, see Fig. 1) [12], and it is also chemically inert which makes it resilient to most chemical attacks [13]. Given these properties, boron carbide is an ideal material for equipment in which superhardness and ultralightweight characteristics are crucial.

However, boron carbide suffers from a major inconvenience which limits its application: at pressures near 40 GPa, it suffers a dramatic drop in shear strength, leading to mechanical performances much poorer than expected [14,15]. This was first demonstrated by shockwave experiments [11,12,14–16] where a kink in the Hugoniot curve near 40 GPa (Fig. 1)—corresponding to the slope of the shock velocity versus particle velocity significantly flattening—is observed. While this feature is widely interpreted as a phase transition [12], it is important to note that alternative explanations have been proposed, such as the pressure-induced formation of point defects, namely vacancies or an interstitial atom in the linear chain [3,17,18]. According to this interpretation, it is those defects that would be responsible for the loss of strength beyond the HEL. A complete description of this viewpoint, as well as others, can be found elsewhere [17]. Nevertheless, the phase transition scenario is often considered responsible for the observed drop in shear strength of boron carbide and is often associated with partial amorphization [19,20]. Indeed, Raman spectroscopy measurements of nanoindented boron carbide evidence the presence of broad modes originating from stress-induced amorphization [9]. Moreover, postmortem analysis

---

[*] Contact author: akliang@eitech.edu.cn
[†] Contact author: Dominique.Laniel@ed.ac.uk

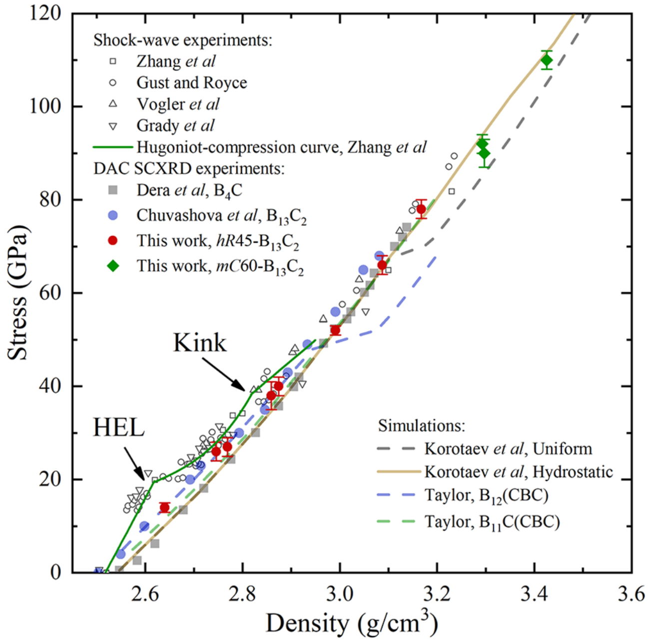

FIG. 1. A compilation of the stress versus density literature data points for different stoichiometry of boron carbide, determined from shock-compression experiments (empty symbols, B_4C was used in all four studies) [12,14–16], static compression experiments (solid symbols) [27,31], and theoretical simulations (solid and dashed lines) [22–24]. The data from this work for the ambient pressure phase (*hR*45-$B_{13}C_2$) and the new high-pressure phase (*mC*60-$B_{13}C_2$) are shown as red circles and green diamonds, respectively. The solid green line represents the Hugoniot compression curve obtained from Zhang *et al.*'s work [12].

of shocked boron carbide with high-resolution electron microscopy experiments confirmed the amorphization, observed in bands parallel to specific crystallographic planes [21].

In order to find pathways to circumvent and control the amorphization of boron carbide, and thus presumably its decrease in shear strength, it is essential to understand the underlying mechanisms. For this purpose, a significant number of density functional theory (DFT) calculations were performed on boron carbides [19,22–25]. These suggest that the C–B–C, C–C–C, or C–B–B linear chains, linking together the icosahedra, bend under both sufficient hydrostatic and nonhydrostatic pressures which causes a phase transition as well as the formation of covalent bonds between atoms of the chain and those of the icosahedra [19,22–25]. Upon further pressure change, whether an increase or a decrease [20], the presence of these newly formed covalent bonds would result in significantly distorting the icosahedra, eventually resulting in the solid's amorphization. Thus, identified as the key mechanism causing boron carbide's amorphization, experimental validation of the presumed pressure-induced bending of the linear chain—and the phase transition leading to it—is of high importance.

In an attempt to experimentally observe chain bending, multiple static compression experiments employing diamond anvil cells (DACs) were performed [26–29]. Two studies reported evidence of a pressure-induced phase transition in $B_{4.3}C$ near 35–40 GPa, based on Raman modes' frequency shifts, intensity analysis, and Grüneisen parameter determination as a function of pressure [28,30]. However, despite many attempts, no sign of such a transformation was observed in other experiments [26,27,29,31], including precise single-crystal x-ray diffraction (SCXRD) measurements on B_4C up to 74 GPa [31] and on $B_{13}C_2$ up to 68 GPa [27] (indicated by solid symbols in Fig. 1). Another set of DAC experiments [20,32] found that, under nonhydrostatic conditions, compressing boron carbide above 25 GPa followed by a pressure release resulted in a partial amorphization, observable only below ∼20 GPa and all the way down to ambient conditions [20]. While molecular dynamics simulations suggest the cause of this behavior to be the bending of the chain [20], the crucial experimental evidence is still lacking.

Here, we present synchrotron SCXRD measurements of boron carbide compressed up to 110(2) GPa in a DAC. These unveil the transformation of hexagonal boron carbide into a monoclinic polymorph featuring the sought-after bent C–B–C chain. The formation of covalent bonds between the chains' atoms and those of the B_{12} icosahedra is observed, and the effect it has on the deformation of the icosahedra as well as the reversibility of the phase transition is investigated.

II. METHODS

In this study, three BX90-type DACs (Fig. S1) with diamond anvil culets of diameter of 250 μm (exp #1) and 120 μm (exp #2 and #3) were prepared to reach pressures of up to 55 and 110 GPa, respectively. Molecular nitrogen was used as the pressure transmitting medium (PTM) and loaded along with commercially available boron carbide (< 10 μm, 98% purity, Sigma Aldrich). Ambient condition SCXRD was performed on several randomly selected single crystals from the commercially purchased boron carbide sample. The unit cell volumes, as summarized in Table S1, ranged from 327.8(1) to 335.2(1) Å^3, indicating the presence of boron carbide with varying stoichiometries. Powder XRD measurements were also conducted on the same sample, and the Le Bail refinement results are consistent with those from SCXRD (Fig. S2). The lattice parameters of the specific crystal loaded into the DAC for high-pressure experiments were not measured at ambient conditions. Instead, the stoichiometry of the loaded sample was estimated to be $B_{13}C_2$ based on its measured equation of state (Figs. 1 and S3), which closely matches the equation of state reported by Chuvashova *et al.* [27]. While evidence suggests the composition of the studied material to be $B_{13}C_2$, the presence of defects—and thereby of a slightly different composition—cannot be ruled out. More detailed crystal structure and stoichiometry analysis of the starting material used in this work can be found in the Supplemental Material [33]. DFT calculations were also performed to provide further insight into boron carbide's behavior. The complete experimental and calculation details can be found in the Supplemental Material [33] (also including Refs. [34–55]).

III. RESULTS AND DISCUSSION

At ambient conditions, boron carbide crystallizes in the trigonal crystal system [space group *R*-3*m*, No. 166, Fig. 2(d)] [5], here denoted by the Pearson notation *hR*45-$B_{13}C_2$. In this study, $B_{13}C_2$ maintained the *hR*45-$B_{13}C_2$ crystal structure up

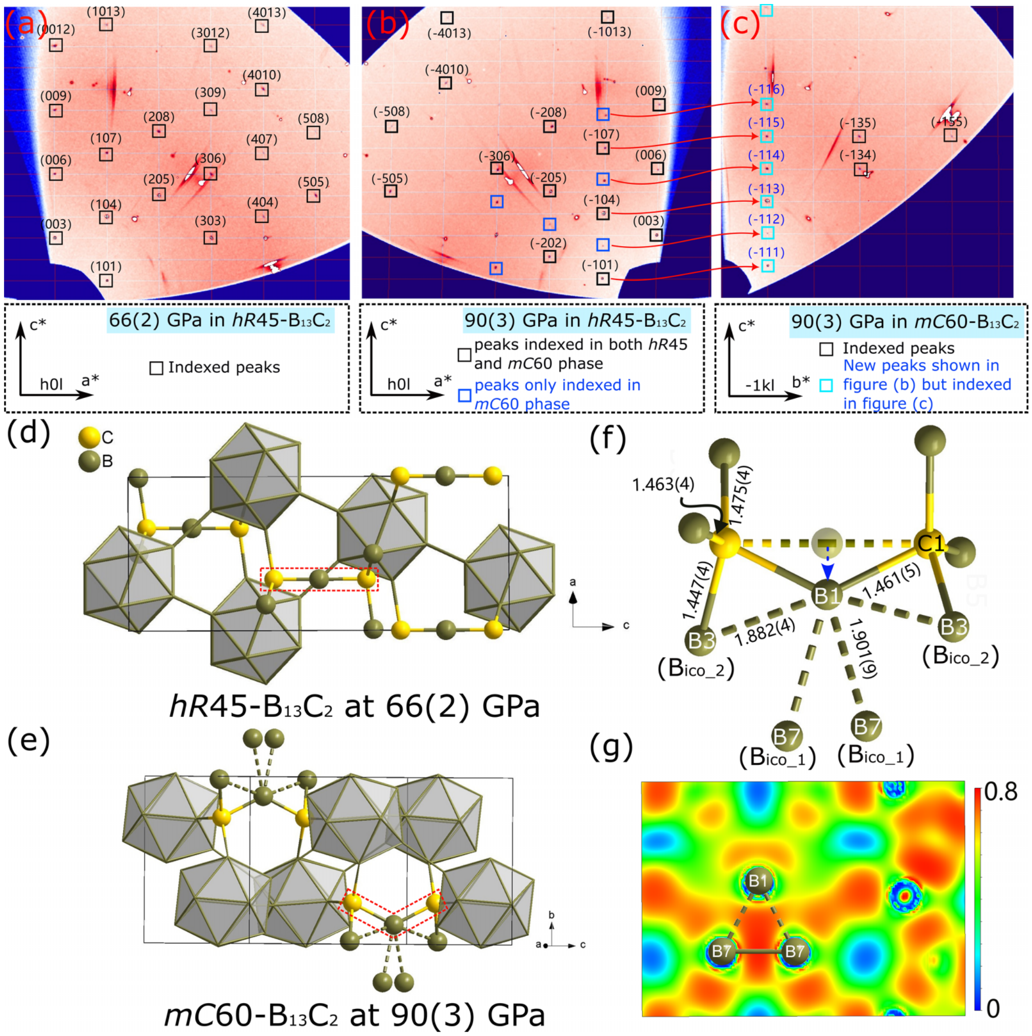

FIG. 2. X-ray diffraction reciprocal-space reconstruction precession image for the (h0l) plane of (a) *h*R45-$B_{13}C_2$ at 66(2) GPa; (b) *m*C60-$B_{13}C_2$ at 90(3) GPa, but imposing the same, and now incorrect, unit cell as in *h*R45-$B_{13}C_2$—enabling to see the new, unexplained reflections (peaks marked by blue squares)—and (c) the (-1kl) plane of *m*C60-$B_{13}C_2$ at 90(3) GPa with the correct monoclinic unit cell that explains the new reflections. The Miller indices of the indexed reflections are marked in black squares while, in (b), the new reflections that do not fit *h*R45-$B_{13}C_2$ are highlighted with blue squares. The crystal structure of (d) *h*R45-$B_{13}C_2$ at 66(2) GPa and (e) *m*C60-$B_{13}C_2$ at 90(3) GPa were obtained from the corresponding SCXRD data (Tables S5 and S7). Boron atoms are represented by dark yellow spheres, carbon atoms by light yellow spheres, and the C–B–C chain is highlighted by red dashed lines. Newly formed weak B–B bonds in the *m*C60-$B_{13}C_2$ phase at 90(3) GPa are shown as dashed lines, while the icosahedra formed by the 12 boron atoms are shown in stick form for clarity. The continuous black line indicates the unit cells. (f) Representation of the C–B–C chain as observed in *h*R45-$B_{13}C_2$ at 66(2) GPa (partly transparent sphere) and *m*C60-$B_{13}C_2$ at 90(3) GPa (solid spheres). (g) Calculated electron localization function (ELF) along a selected plane at 90 GPa (see also Fig. S16). The bond distances, obtained from the experimental data, are provided in angstrom (Å).

to 78(2) GPa—consistent with previous SCXRD experiments on $B_{13}C_2$ [27] and B_4C [31], where no phase transition was detected up to pressures of 68 and 74 GPa, respectively. The here-obtained measurements on *h*R45-$B_{13}C_2$ are summarized in Table S2 and Fig. S4 [33]. The structure refinement results, quality factors, atomic position and structure models of *h*R45-$B_{13}C_2$ at various pressures are detailed in Tables S3–S6 [33], and the here-obtained structure solution is consistent with the literature [5]. The crystal structure solved and refined at 66(2) GPa is shown in Fig. 2(d). As previously described [5], it features a three-dimensional framework of twelve-boron-atom icosahedra connected by B–B bonds and straight C–B–C chains, together forming a network of covalently bonded chains and clusters.

When compressing *h*R45-$B_{13}C_2$ at ambient temperature beyond 78(2) GPa, namely at 90(3) GPa (exp #3) and above, SCXRD measurements revealed the presence of new diffraction peaks. Indeed, attempting to use the unit cell of *h*R45-$B_{13}C_2$ to explain the SCXRD data at 90(3) GPa results in many peaks not adhering to the unit cell and systematic absences of space group R-3m [Fig. 2(b), e.g., $-$h + k + l = 3n (n = 0,1,2,3 …)], demonstrating the occurrence of a phase transition. The same new phase was also observed from exp #2 after laser-heating to temperatures of 2600(200) and 2800(200) K at 92(2) and 110(2) GPa. Under these conditions, boron carbide may have melted [7,8], followed by its quenching to room temperature. This new phase was solved and refined. It was found to preserve the $B_{13}C_2$

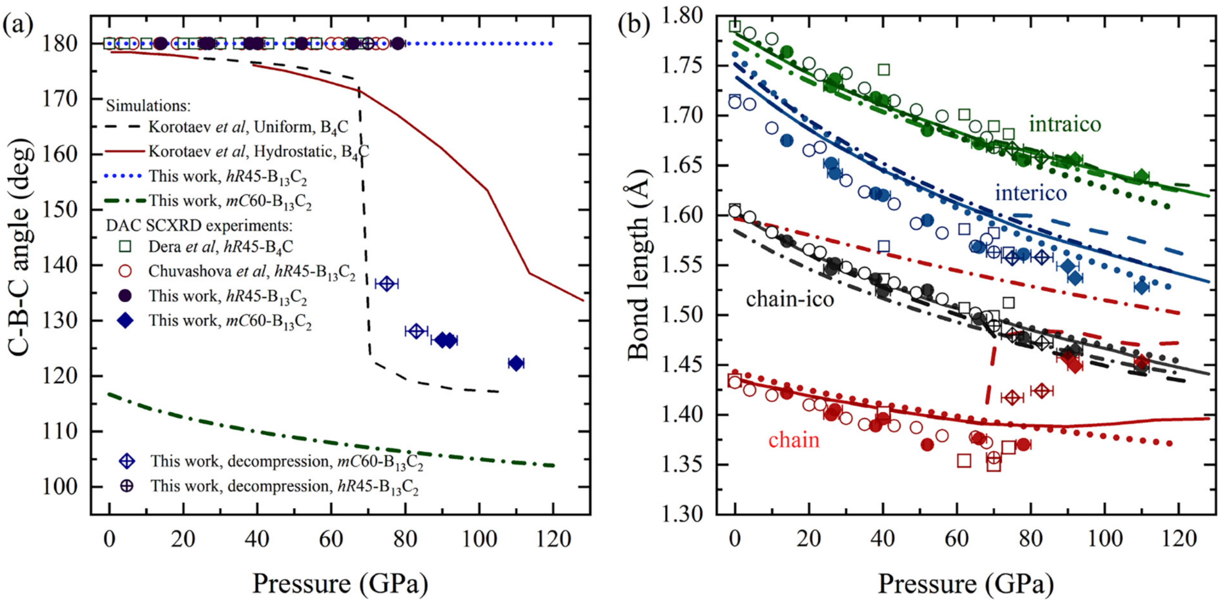

FIG. 3. Pressure dependence of the chain angle and bond lengths in boron carbide. Pressure dependence of (a) the C–B–C chain angle, and (b) the average B–B bond length of the B_{12} icosahedra (intraico) and between B_{12} icosahedra (interico), the average B–C bond length where the B is part of the B_{12} icosahedra (chain-ico), and between B and C atoms from the C–B–C chain (chain) [see Fig. 2(f)]. Calculation results are shown as solid or dashed lines in all figures, while experimental data is shown as empty or solid symbols. The symbols representing data in (a) are applied to (b) but with other colors. For comparison, the figure includes simulation results from Korotaev *et al.* on B_4C [22,23], experimental results from Dera *et al.* on *hR*45-B_4C [31], and experimental results from Chuvashova *et al.* on *hR*45-$B_{13}C_2$ [27]. The uncertainty in the chain angle and bond distance values presented here is smaller than the symbol size.

stoichiometry but to adopt a monoclinic *C*-centered Bravais lattice (space group *C*2/*c*, No. 15, Fig. 2(e), hereafter referred to as *mC*60-$B_{13}C_2$). The lattice parameters at 90(3) GPa are $a = 9.050(2)$ Å, $b = 5.056(2)$ Å, $c = 7.943(2)$ Å and $\beta = 114.21(3)°$, with a unit cell volume of 331.5(2) $Å^3$. The reciprocal space reconstruction image of the (-1kl) plane for the *mC*60-$B_{13}C_2$ phase at 90(3) GPa is shown in Fig. 2(c). The latter allows to see that this monoclinic unit cell explains peaks that could not be indexed with the unit cell of *hR*45-$B_{13}C_2$. The lattice parameters, refinement results, quality factors, and crystal structure of *mC*60-$B_{13}C_2$ at 90(3), 92(2), and 110(2) GPa are detailed in Tables S7 and S8 [33]. Raman spectroscopy measurements confirm the presence of new Raman modes that can be assigned to *mC*60-$B_{13}C_2$ (Figs. S5–S7). The full discussion of the Raman measurements is presented in the Supplemental Material [33].

In *mC*60-$B_{13}C_2$, there is a total of eight crystallographically distinct atoms; one carbon and seven boron. Six boron atoms are located on the 8*f* Wyckoff position, forming the B_{12} icosahedra, while the remaining boron atom is located at the 4*e* Wyckoff position. This atom bonds with the carbon atoms at the 8*f* Wyckoff position, together forming C–B–C chains [Fig. 2(e)]. The structure that those atoms form has obvious similarities to *hR*45-$B_{13}C_2$ (Fig. 2). Indeed, *mC*60-$B_{13}C_2$ is also comprised of B_{12} icosahedra interlinked through B–B bonds and C–B–C chains. However, there is a remarkable difference between the *hR*45-$B_{13}C_2$ and *mC*60-$B_{13}C_2$ polymorphs: the bent C–B–C chain in the latter [Figs. 2(e) and 2(f)]. Indeed, the chain angle decreases from 180° at 78(2) GPa in *hR*45-$B_{13}C_2$ to 126.5(8)° at 90(3) GPa in *mC*60-$B_{13}C_2$ [Fig. 3(a)]. Another consequence of the chain bending is the elongation of the chain's B–C bond lengths, shifting from 1.370(2) Å at 78(2) GPa to 1.457(6) Å at 90(3) GPa [Fig. 3(b)].

To corroborate the obtained crystal structure, DFT calculations were performed on the *mC*60-$B_{13}C_2$ polymorph, as well as *hR*45-$B_{13}C_2$, at pressures ranging from 0 to 200 GPa. The calculated atomic positions, lattice parameters, and volumes agreed with the values obtained from SCXRD experiments (see Tables S8–S12 and Fig. S8 for data up to 120 GPa). Furthermore, the pressure-induced abrupt decrease in the C–B–C angles and the elongation of the C–B bond length within the C–B–C chain, as observed in our SCXRD experiments, are not only reproduced by our calculations but also show good agreement with the predictions from previous molecular dynamics simulations (Fig. 3) [22,23]. A detailed analysis of the experimental structure model of *mC*60-$B_{13}C_2$ and its calculated phonon dispersion curves suggests the presence of mild static disorder in the B atom's position within the C–B–C chain (B_{chain}; c.f. Figs. S10–S14 and related analysis as well as discussion in the Supplemental Material [33]). The chain bending in boron carbide, whether $B_{13}C_2$ or B_4C, has been hypothesized to be responsible for its partial amorphization, resulting in a significant deterioration of its mechanical properties [19,24]. The proposed mechanism from which chain bending induces amorphization is through the formation of B–B bonds between boron atoms from the icosahedra and from the chain. The presence of these bonds would significantly distort the icosahedra upon pressure decrease or increase, eventually resulting in the solid's amorphization [20]. As such, it is of capital importance to assess whether or not atoms which are part of the bent C–B–C chain form some covalent bonds with atoms constituting the icosahedra. Based on experimental data at 90(3) GPa, two crystallographically distinct B atoms in the B_{12} icosahedra (B3 and B7 in Fig. 2(f), hereafter referred to as B_{ico_2} and B_{ico_1}, respectively) are in close proximity to the B_{chain} atom (B1) in $mC60$-$B_{13}C_2$. Indeed, the bond distances between them are 1.901(9) and 1.882(4) Å, respectively. This implies an abrupt contraction in these interatomic distances following the phase transition, as the $B_{chain} - B_{ico\_1}$ and $B_{chain} - B_{ico\_2}$ were 2.140(1) and 2.712(1) Å at 78(2), respectively GPa (Fig. S15). The short B–B distances in $mC60$-$B_{13}C_2$ strongly suggest the formation of covalent bonds as they approach the value of B–B bonded atoms in $hR45$-$B_{13}C_2$ at ambient conditions (1.8053(4) Å) [56] and are even shorter than the intraicosahedra bonds in α-B (1.987(2) Å) at 5.7(5) GPa [57]. To further assess the presence of covalent bonding between the B_{chain} and those in the B_{12} icosahedra in the $mC60$-$B_{13}C_2$ phase, the electron localization function (ELF) was calculated. Remarkably, at 90 GPa, the ELF values at the critical bond distance (the bond center) between B_{chain} and the B_{ico_1}/B_{ico_2} atoms are 0.89 and 0.77 (Fig. 2(g) and Fig. S16), respectively, indicating covalent bonding [58].

With the presence of these important bonds established, it is now necessary to determine if these distort the B_{12} cages. For this, the Baur distortion index (BDI) was calculated for the B_{12} icosahedra, as described in the Supplemental Material [33]. For the $mC60$-$B_{13}C_2$ phase, this yielded values of 0.0101(6), 0.0102(8), and 0.0118(9) at pressures of 90(3), 92(2), and 110(2) GPa (Fig. S17), respectively, indicating only a slightly greater distortion compared to that of the $hR45$-$B_{13}C_2$ phase (an average of 0.007 04 up to 78(2) GPa). This mild increase is likely due to the greater number of crystallographically distinct atoms comprising the icosahedra in $mC60$-$B_{13}C_2$ compared to $hR45$-$B_{13}C_2$. As such, this analysis suggests that the formation of bonds between the B_{chain} atom and the B_{ico} atoms does not result in a significant distortion of the B_{12} cages which would lead to amorphization upon compression. Moreover, SCXRD and Raman spectroscopy (Figs. S6 and S7) investigation of the $mC60$-$B_{13}C_2$ phase upon a slow decompression (~6 hours) shows that $B_{13}C_2$ remains in the $mC60$-$B_{13}C_2$ phase down to 75(3) GPa but, remarkably, transforms back into the $hR45$-$B_{13}C_2$ phase at 70(2) GPa (Table S2). The reversible nature of the phase transition, along with the restoration of the B_{12} icosahedra's BDI (Fig. S17), further strengthens the claim that, for boron carbide samples compressed under quasihydrostatic conditions, the chain bending is unlikely to be the mechanism that results in decompression-induced amorphization.

Beyond the static disorder detected in $mC60$-$B_{13}C_2$, analysis of the SCXRD data does not reveal the presence of defects, whether vacancies or interstitial atoms. However, these have been suggested to potentially play an important role [17,18]. Of particular relevance here, recent DFT calculations [2] have found the nonmonotonic pressure evolution of a Raman mode centered near 270 cm^{-1} [28] to potentially be due to defect C–B–C–B chains in B_4C-type boron carbide. As shown in Fig. S5, this mode is present in our commercially obtained samples (near 235 cm^{-1} at 23.3 GPa). As such, if this mode is confirmed to indeed be the unambiguous signature of defect C–B–C–B chains [2], their exact role in the phase transition here observed would need to be considered in detail.

Nonetheless, for the formation of the $mC60$-$B_{13}C_2$ boron carbide polymorph to be primarily driven by defects appears unlikely. Indeed, it can be noted that the presence and effects of presumed C–B–C–B chains were not captured or reflected in the average unit cell of $hR45$-$B_{13}C_2$. As such, it is reasonable to expect that their effects are also not observed in the average unit cell of the $mC60$-$B_{13}C_2$ polymorph, meaning that the obtained average structure model is not mainly due to these defects. Moreover, the successful formation of the $mC60$-$B_{13}C_2$ compound after laser-heating, with high temperatures being conducive to the removal of defects [56], as well as the fully reversible nature of the phase transition with minimal hysteresis, all point to the $hR45$-$B_{13}C_2$ to $mC60$-$B_{13}C_2$ transition to be driven by thermodynamics rather than kinetics.

From the diffraction data discussed above, the bulk modulus of $hR45$-$B_{13}C_2$ was determined from a third-order Birch-Murnaghan equation of state (BM3 EoS) fit [59,60] (Fig. S18). Values of $B_0 = 236(7)$ GPa, $B'_0 = 3.0(3)$ and $V_0/Z = 109.08$ Å^3 (fixed, from Ref. [56]), and of $B_0 = 227.6(12)$ GPa, $B'_0 = 3.38(2)$ and $V_0/Z = 111.33(5)$ Å^3 from DFT calculations, were obtained. These are in good agreement with previously reported values [$B_0 = 239(7)$ GPa and $B'_0 = 3.2(3)$] [27]. For the $mC60$-$B_{13}C_2$ phase, the small number of experimental data points does not allow the extraction of reliable EoS parameters. However, the bulk modulus and its pressure derivative calculated from DFT are 238.4(6) GPa and 3.42(1) ($V_0/Z = 107.70(2)$ Å^3), respectively, both of which are slightly higher than the calculated values for the $hR45$-$B_{13}C_2$ phase. It is interesting to note that the $mC60$-$B_{13}C_2$ data points fall clearly below the extrapolated BM3 EoS of the $hR45$-$B_{13}C_2$ phase. This suggests a volume discontinuity between the polymorphs (Fig. S18, of about 1.3% at 90 GPa), which could point to the phase transition being of the first order. This is also supported by the fact that there is no group-subgroup relationship between $hR45$-$B_{13}C_2$ and $mC60$-$B_{13}C_2$, which are only related through the intermediate space groups P-3m1 (No. 164), $P2/m$ (No. 10), or R-3 (No. 148) (Fig. S19).

IV. CONCLUSIONS

In conclusion, a pressure-induced phase transition has been observed in $B_{13}C_2$ boron carbide at pressures between 78(2) and 90(3) GPa. The crystal structure of the new phase, $mC60$-$B_{13}C_2$, was determined using synchrotron SCXRD and features a bent C–B–C chain. Remarkably, the B atom of this chain is shown from experiments and DFT calculations to form covalent bonds with the B atoms of the two neighboring icosahedra. However, these bonds do not seem to meaningfully distort the B_{12} cages and, upon decompression, $mC60$-$B_{13}C_2$ reverts to $hR45$-$B_{13}C_2$. Based on this behavior, the chain bending seems unlikely to induce the previously detected amorphization. Still, it is worth noting that the phase transition pressure observed here between the two polymorphs agrees well with the values obtained from molecular dynamics simulations under hydrostatic conditions, which predict a transition above 72 GPa to a structure with a bent chain [22,23]. However, this pressure value is higher than the one obtained from experiments and calculations for boron carbide under shock compression (40–50 GPa) [12,14–16,24]. This discrepancy could be due to differences between uniaxial load and hydrostatic conditions, with the phase here observed likely to be the same phase as the one detected during shock compression. These findings are essential for shedding light on the phase transition observed in multiple shock-wave experiments and the failure in the strength of boron carbide, but also to help understanding the mechanisms playing a role in the amorphization of boron carbide under stress.

Future studies reproducing these experiments albeit with an boron carbide sample established to be essentially defect-free [56] would permit the generalization of a $hR45\text{-}B_{13}C_2$ to $mC60\text{-}B_{13}C_2$ phase transition in boron carbides.

ACKNOWLEDGMENTS

We acknowledge the European Synchrotron Radiation Facility (ESRF) for provision of beamtime at the ID11 beamlines under Proposals No. HC-5390, No. HC-5589, and No. CH-6821. We acknowledge DESY (Hamburg, Germany), a member of the Helmholtz Association HGF, for the provision of experimental facilities. Parts of this research were carried out at PETRA III. Data was collected at the P02.2 beamline operated by DESY Photon Science. Beamtime was allocated for Proposals No. I-20230832, No. I-20230064, and No. I-20240286. The authors thank Rebecca Rae for her assistance with the collection of the powder x-ray diffraction data using a laboratory diffractometer. D.L., A.L., and U.R. thank the UKRI Future Leaders Fellowship (MR/V025724/1) for financial support. F.T. acknowledges support through ERC Grant (UNMASCC-HP, 10.3030/101117758). This work was funded by the European Union. F.T. acknowledges further the Swedish government's Strategic Research Area in Materials Science on Functional Materials at Linköping University (faculty grant SFO-Mat-LiU 2009-00971). Computations were enabled by resources provided by the National Academic Infrastructure for Supercomputing in Sweden (NAISS), partially funded by the Swedish Research Council through Grant Agreement No. 2022–06725. We acknowledge NAISS for providing access to the LUMI supercomputer, owned by the EuroHPC Joint Undertaking and hosted by CSC (Finland) and the LUMI consortium.

Views and opinions expressed are however those of the author(s) only and do not necessarily reflect those of the European Union or the European Research Council Executive Agency. Neither the European Union nor the granting authority can be held responsible for them.

DATA AVAILABILITY

The data that support the findings of this article are openly available [61].

[1] F. Igoa Saldaña, T. Gaudisson, S. Le Floch, B. Baptiste, L. Delbes, V. Malarewicz, O. Beyssac, K. Béneut, C. Coelho Diogo, C. Gervais, *et al.*, Transforming nanocrystals into superhard boron carbide nanostructures, ACS Nano **18**, 30473 (2024).

[2] A. Jay, O. Hardouin Duparc, J. Sjakste, and N. Vast, Theoretical Raman spectrum of boron carbide $B_{4.3}C$ under pressure, Acta Mater. **255**, 119085 (2023).

[3] A. Jay, O. Hardouin Duparc, J. Sjakste, and N. Vast, Theoretical phase diagram of boron carbide from ambient to high pressure and temperature, J. Appl. Phys. **125**, 185902 (2019).

[4] K. Rasim, R. Ramlau, A. Leithe-Jasper, T. Mori, U. Burkhardt, H. Borrmann, W. Schnelle, C. Carbogno, M. Scheffler, and Y. Grin, Local atomic arrangements and band structure of boron carbide, Angew. Chem. **130**, 6238 (2018).

[5] H. K. Clark and J. L. Hoard, The crystal structure of boron carbide, J. Am. Chem. Soc. **65**, 2115 (1943).

[6] A. Courac, V. Turkevich, and Y. Le Godec, Thermodynamics and crystallography of hard light-element boron-rich compounds by *in situ* x-ray diffraction under high-pressure, high-temperature conditions, Solid State Sci. **163**, 107909 (2025).

[7] A. Courac, Y. Le Godec, J. Sjakste, N. Vast, O. Rapaud, and V. Turkevich, High-pressure, high-temperature phase equilibria with superhard boron-rich compounds of B–C–N–O and B–C–Si systems by *in situ* x-ray diffraction and CALPHAD methodology, ACS Appl. Mater. Interfaces **17**, 53013 (2025).

[8] J. D. Coe, C.-F. Chen, C. W. Greeff, D. M. Dattelbaum, J. T. Gammel, B. L. Musicó, C. A. McCoy, P. Kalita, and B. A. Branch, Equation of state of boron carbide B_4C, Phys. Rev. B **112**, 094106 (2025).

[9] V. Domnich, Y. Gogotsi, M. Trenary, and T. Tanaka, Nanoindentation and Raman spectroscopy studies of boron carbide single crystals, Appl. Phys. Lett. **81**, 3783 (2002).

[10] T. Francois, Boron carbide—a comprehensive review, J. Eur. Ceram. Soc. **6**, 205 (1990).

[11] D. E. Grady, Hugoniot equation of state and dynamic strength of boron carbide, J. Appl. Phys. **117**, 165904 (2015).

[12] Y. Zhang, T. Mashimi, T. Uemura, M. Uchino, M. Kodama, K. Shibata, K. Fukuoka, M. Kikuchi, T. Kobayashi, and T. Sekine, Shock compression behaviors of boron carbide (B_4C), J. Appl. Phys. **100**, 113536 (2006).

[13] S. Song, W. Xu, R. Cao, L. Luo, M. H. Engelhard, M. E. Bowden, B. Liu, L. Estevez, C.-M. Wang, and J.-G. Zhang, B_4C as a stable non-carbon-based oxygen electrode material for lithium-oxygen batteries, Nano Energy **33**, 195 (2017).

[14] T. J. Vogler, W. D. Reinhart, and L. C. Chhabildas, Dynamic behavior of boron carbide, J. Appl. Phys. **95**, 4173 (2004).

[15] D.E. Grady, Shock-wave strength properties of boron carbide and silicon carbide, J. Phys. IV France **04**, C8-385 (1994).

[16] W. H. Gust and E. B. Royce, Dynamic yield strengths of B_4C, BeO, and Al_2O_3 ceramics, J. Appl. Phys. **42**, 276 (1971).

[17] A. Chakraborti, A. Jay, O. Hardouin Duparc, J. Sjakste, K. Béneut, N. Vast, and Y. Le Godec, Boron carbide under

torsional deformation: Evidence of the formation of chain vacancies in the plastic regime, Acta Mater. **226**, 117553 (2022).

[18] R. Raucoules, N. Vast, E. Betranhandy, and J. Sjakste, Mechanical properties of icosahedral boron carbide explained from first principles, Phys. Rev. B **84**, 014112 (2011).

[19] S. Aryal, P. Rulis, and W. Y. Ching, Mechanism for amorphization of boron carbide B_4C under uniaxial compression, Phys. Rev. B **84**, 184112 (2011).

[20] X. Q. Yan, Z. Tang, L. Zhang, J. J. Guo, C. Q. Jin, Y. Zhang, T. Goto, J. W. McCauley, and M. W. Chen, Depressurization amorphization of single-crystal boron carbide, Phys. Rev. Lett. **102**, 075505 (2009).

[21] M. Chen, J. W. Mccauley, and K. J. Hemker, Shock-induced localized amorphization in boron carbide, Science **299**, 1563 (2003).

[22] P. Korotaev, P. Pokatashkin, and A. Yanilkin, Structural phase transitions in boron carbide under stress, Model. Simul. Mat. Sci. Eng. **24**, 015004 (2016).

[23] P. Korotaev, P. Pokatashkin, and A. Yanilkin, The role of non-hydrostatic stresses in phase transitions in boron carbide, Comput. Mater. Sci. **121**, 106 (2016).

[24] D. E. Taylor, Shock compression of boron carbide: A quantum mechanical analysis, J. Am. Ceram. Soc. **98**, 3308 (2015).

[25] Q. An, W. A. Goddard, III, and T. Cheng, Atomistic explanation of shear-induced amorphous band formation in boron carbide, Phys. Rev. Lett. **113**, 095501 (2014).

[26] I. Chuvashova, B. Gasharova, Y. L. Mathis, L. Dubrovinsky, and N. Dubrovinskaia, Structural stability of boron carbide under pressure proven by spectroscopic studies up to 73 GPa, Z. Anorg. Allg. Chem. **643**, 1357 (2017).

[27] I. Chuvashova, E. Bykova, M. Bykov, V. Svitlyk, L. Dubrovinsky, and N. Dubrovinskaia, Structural stability and mechanism of compression of stoichiometric $B_{13}C_2$ up to 68 GPa, Sci. Rep. **7**, 8969 (2017).

[28] A. Hushur, M. H. Manghnani, H. Werheit, P. Dera, and Q. Williams, High-pressure phase transition makes $B_{4.3}C$ boron carbide a wide-gap semiconductor, J. Phys. Condens. Matter **28**, 045403 (2016).

[29] T. Fujii, Y. Mori, H. Hyodo, and K. Kimura, X-ray diffraction study of B_4C under high pressure, J. Phys. Conf. Ser. **215**, 012011 (2010).

[30] H. Werheit, M. H. Manghnani, U. Kuhlmann, A. Hushur, and S. Shalamberidze, Mode Grüneisen parameters of boron carbide, Solid State Sci. **72**, 80 (2017).

[31] P. Dera, M. H. Manghnani, A. Hushur, Y. Hu, and S. Tkachev, New insights into the enigma of boron carbide inverse molecular behavior, J. Solid State Chem. **215**, 85 (2014).

[32] R. Sereika, S. Iwan, P. A. Baker, and Y. K. Vohra, High pressure Raman spectroscopy of boron-rich boron carbides up to 50 GPa, High. Press. Res. **45**, 79 (2025).

[33] See Supplemental Material at http://link.aps.org/supplemental/10.1103/v5kf-svcz for detailed experimental and computational methods, discussion of the structure and stoichiometry determination, Raman spectra analysis, partial disorder of the C–B–C chain in the $mC60$-$B_{13}C_2$ phase, and the complete set of supplementary tables and figures.

[34] The phonon band structures to be visualized on the website, https://henriquemiranda.github.io/phononwebsite/phonon.html (2025).

[35] D. Laniel, F. Trybel, A. Aslandukov, J. Spender, U. Ranieri, T. Fedotenko, K. Glazyrin, E. L. Bright, S. Chariton, V. B. Prakapenka, *et al.*, Structure determination of zeta-N_2 from single-crystal x-ray diffraction and theoretical suggestion for the formation of amorphous nitrogen, Nat. Commun. **14**, 6207 (2023).

[36] P. Giannozzi, O. Baseggio, P. Bonfa, D. Brunato, R. Car, I. Carnimeo, C. Cavazzoni, S. de Gironcoli, P. Delugas, F. Ferrari Ruffino, *et al.*, Quantum ESPRESSO toward the exascale, J. Chem. Phys. **152**, 154105 (2020).

[37] Single crystal diffraction software CrysAlis$^{\text{Pro}}$, Rigaku Journal, **32**, 31 (2016).

[38] X. Yang, W. A. Goddard, and Q. An, Structure and properties of boron-very-rich boron carbides: B_{12} icosahedra linked through bent CBB chains, J. Phys. Chem. C **122**, 2448 (2018).

[39] P. Giannozzi, O. Andreussi, T. Brumme, O. Bunau, M. Buongiorno Nardelli, M. Calandra, R. Car, C. Cavazzoni, D. Ceresoli, M. Cococcioni, *et al.*, Advanced capabilities for materials modelling with Quantum ESPRESSO, J. Phys. Condens. Matter **29**, 465901 (2017).

[40] J. M. Skelton, L. A. Burton, S. C. Parker, A. Walsh, C.-E. Kim, A. Soon, J. Buckeridge, A. A. Sokol, C. R. A. Catlow, A. Togo, *et al.*, Anharmonicity in the high-temperature *Cmcm* phase of SnSe: Soft modes and three-phonon interactions, Phys. Rev. Lett. **117**, 075502 (2016).

[41] A. Togo and I. Tanaka, First principles phonon calculations in materials science, Acta Mater. **108**, 1 (2015).

[42] G. M. Sheldrick, SHELXT-Integrated space-group and crystal-structure determination, Acta Crystallogr. **71**, 3 (2015).

[43] K. Shirai, K. Sakuma, and N. Uemura, Theoretical study of the structure of boron carbide $B_{13}C_2$, Phys. Rev. B **90**, 064109 (2014).

[44] H. Werheit and U. Kuhlmann, Superconductivity in boron carbide? Clarification by low-temperature MIR/FIR spectra, J. Phys. Condens. Matter **23**, 435501 (2011).

[45] K. Momma and F. Izumi, VESTA 3 for three-dimensional visualization of crystal, volumetric and morphology data, J. Appl. Crystallogr. **44**, 1272 (2011).

[46] V. Domnich, S. Reynaud, R. A. Haber, and M. Chhowalla, Boron carbide: Structure, properties, and stability under stress, J. Am. Ceram. Soc. **94**, 3605 (2011).

[47] J. Guo, L. Zhang, T. Fujita, T. Goto, and M. Chen, Pressure-induced depolarization and resonance in Raman scattering of single-crystalline boron carbide, Phys. Rev. B **81**, 060102(R) (2010).

[48] S. Grimme, J. Antony, S. Ehrlich, and H. Krieg, A consistent and accurate *ab initio* parametrization of density functional dispersion correction (DFT-D) for the 94 elements H-Pu, J. Chem. Phys. **132**, 154104 (2010).

[49] P. Giannozzi, S. Baroni, N. Bonini, M. Calandra, R. Car, C. Cavazzoni, D. Ceresoli, G. L. Chiarotti, M. Cococcioni, I. Dabo, *et al.*, QUANTUM ESPRESSO: A modular and open-source software project for quantum simulations of materials, J. Phys. Condens. Matter **21**, 395502 (2009).

[50] O. V. Dolomanov, L. J. Bourhis, R. J. Gildea, J. A. K. Howard, and H. Puschmann, OLEX2: A complete structure solution, refinement and analysis program, J. Appl. Crystallogr. **42**, 339 (2009).

[51] A. Dewaele, P. Loubeyre, and M. Mezouar, Equations of state of six metals above 94 GPa, Phys. Rev. B **70**, 094112 (2004).

[52] M. Calandra, N. Vast, and F. Mauri, Superconductivity from doping boron icosahedra, Phys. Rev. B **69**, 224505 (2004).

[53] J. P. Perdew, K. Burke, and M. Ernzerhof, Generalized gradient approximation made simple, Phys. Rev. Lett. **77**, 3865 (1996).

[54] P. E. Blöchl, Projector augmented-wave method, Phys. Rev. B **50**, 17953 (1994).

[55] T. L. Aselage and R. G. Tissot, Lattice constants of boron carbides, J. Am. Chem. Soc. **75**, 2207 (1992).

[56] S. Mondal, E. Bykova, S. Dey, S. I. Ali, N. Dubrovinskaia, L. Dubrovinsky, G. Parakhonskiy, and S. van Smaalen, Disorder and defects are not intrinsic to boron carbide, Sci. Rep. **6**, 19330 (2016).

[57] I. Chuvashova, E. Bykova, M. Bykov, V. Svitlyk, B. Gasharova, Y.-L. Mathis, R. Caracas, L. Dubrovinsky, and N. Dubrovinskaia, High-pressure behavior of α-boron studied on single crystals by x-ray diffraction, Raman and IR spectroscopy, J. Solid State Chem. **245**, 50 (2017).

[58] A. Savin, R. Nesper, S. Wengert, and T. F. Fässler, ELF: The electron localization function, Angew. Chem. Int. Ed. **36**, 1808 (1997).

[59] F. D. Murnaghan, The compressibility of media under extreme pressures, Proc. Natl. Acad. Sci. USA **30**, 244 (1944).

[60] F. Birch, Finite elastic strain of cubic crystals, Phys. Rev. **71**, 809 (1947).

[61] The phonon dispersion files can be found at https://doi.org/10.6084/m9.figshare.30207958; https://doi.org/10.6084/m9.figshare.30208117.